The Meteoritical Society

Meteoritics & Planetary Science 45, Nr 9, 1409–1428 (2010)
doi: 10.1111/j.1945-5100.2010.01104.x

Comet 81P/Wild 2: The size distribution of finer (sub-10 μm) dust collected by the Stardust spacecraft

M. C. PRICE[1*], A. T. KEARSLEY[2], M. J. BURCHELL[1], F. HÖRZ[3], J. BORG[4], J. C. BRIDGES[5], M. J. COLE[1], C. FLOSS[6], G. GRAHAM[2], S. F. GREEN[7], P. HOPPE[8], H. LEROUX[9], K. K. MARHAS[6†], N. PARK[10], R. STROUD[11], F. J. STADERMANN[6], N. TELISCH[12], and P. J. WOZNIAKIEWICZ[12]

[1]School of Physical Sciences, University of Kent, Canterbury CT2 7NH, UK
[†]Present address: Planetary Sciences Division, Physical Research Laboratory, Ahmedabad, Gujarat 38009, India
[2]IARC, Department of Mineralogy, Natural History Museum, London SW7 5BD, UK
[3]LZ Technology/ESCG, NASA Johnson Space Center, Houston, Texas 77058, USA
[4]Institut d'Astrophysique Spatiale, Campus, 91405 Orsay Cedex, France
[5]Space Research Centre, Department of Physics and Astronomy, University of Leicester, Leicester LE1 7RH, UK
[6]Laboratory for Space Sciences, Physics Department, Washington University, Saint Louis, Missouri 63130, USA
[7]PSSRI, The Open University, Milton Keynes MK7 6AA, UK
[8]Max-Planck Institute for Chemistry, P.O. Box 3060, 55020 Mainz, Germany
[9]Unité Matériaux et Transformation, Université de Lille 1, F-59655 Villeneuve d'Ascq, France
[10]AWE, Aldermaston, Reading, Berkshire RG7 4PR, UK
[11]Naval Research Laboratory, Washington, District of Columbia 20375, USA
[12]Institute of Geophysics and Planetary Physics, Lawrence Livermore National Laboratory, 7000 East Avenue, California 94550, USA
[*]Corresponding author. E-mail: mcp2@star.kent.ac.uk

(Received 12 December 2009; revision accepted 29 June 2010)

Abstract–The fluence of dust particles <10 μm in diameter was recorded by impacts on aluminum foil of the NASA Stardust spacecraft during a close flyby of comet 81P/Wild 2 in 2004. Initial interpretation of craters for impactor particle dimensions and mass was based upon laboratory experimental simulations using projectiles less than >10 μm in diameter and the resulting linear relationship of projectile to crater diameter was extrapolated to smaller sizes. We now describe a new experimental calibration program firing very small monodisperse silica projectiles (470 nm–10 μm) at approximately 6 km s^{-1}. The results show an unexpected departure from linear relationship between 1 and 10 μm. We collated crater measurement data and, where applicable, impactor residue data for 596 craters gathered during the postmission preliminary examination phase. Using the new calibration, we recalculate the size of the particle responsible for each crater and hence reinterpret the cometary dust size distribution. We find a greater flux of small particles than previously reported. From crater morphology and residue composition of a subset of craters, the internal structure and dimensions of the fine dust particles are inferred and a "maximum-size" distribution for the subgrains composing aggregate particles is obtained. The size distribution of the small particles derived directly from the measured craters peaks at approximately 175 nm, but if this is corrected to allow for aggregate grains, the peak in subgrain sizes is at <100 nm.

INTRODUCTION

Micrometer and smaller scale dust within cometary comae can be observed by telescopic remote sensing spectroscopy (e.g., Hanner and Bradley 2004; Levasseur-Regourd et al. 2007) and the particle size and abundance can be measured by in situ spacecraft impact detectors (e.g., comet 1P/Halley by McDonnell et al.

1987 and 26P/Grigg-Skjellerup by McDonnell et al. 1993). The NASA Stardust spacecraft made measurements in real time during its flyby of comet 81P/Wild 2 in 2004 using the on-board dust flux monitor instrument (DFMI; Green et al. 2004; Tuzzolino et al. 2004), and also returned samples to Earth for subsequent analysis. An additional measurement was made during the flyby of the cumulative dust flux by an impact ionization detector (cometary and interstellar dust analyzer [CIDA]). At small (1 μm) scales, CIDA (Kissel et al. 2004) reported a cumulative flux significantly lower than that from both DFMI and the returned samples.

Initial interpretation of the size distribution for Stardust samples during preliminary examination (PE; Brownlee et al. 2006) was based upon comparison of aerogel track and aluminum (Al) crater sizes to laboratory calibration data (e.g., Kearsley et al. 2006; Burchell et al. 2008). This appeared to show that very fine dust is relatively sparse with a low negative power function describing the grain size distribution (Hörz et al. 2006; Burchell et al. 2008), and only contributes a small fraction of the solid mass (Kearsley et al. 2008a). Our earlier calibrations using impacting particles >10 μm in diameter have proven useful for interpretation of both aerogel tracks and Al craters, yielding overlapping and comparable data sets from the two substrates. However, for smaller sized particles (especially <1 μm), aerogel track dimensions become difficult to measure by the protocols employed during Stardust cometary PE, and grain size determination has had to rely upon scanning electron microscopy (SEM) to find and measure small impact craters on Al foils. Although there is good correspondence between results from the DFMI and the returned samples for particles above 50 μm diameter (see fig. 4 of Hörz et al. 2006), divergence between the two data sets becomes apparent at smaller sizes, especially below 10 μm, where greater dust fluence is indicated by the DFMI, resulting in a steeper power law describing the particle size distribution.

Can we explain this discrepancy? DFMI calibration is described in Tuzzolino et al. (2003), and there is no evidence of malfunction in the operation of DFMI during passage through the coma (Green, personal communication). Although the returned samples provide a permanent record of the accumulated dust fluence and can be used in diverse postflight investigations, their reliable interpretation (e.g., an impactor size distribution [ISD]) requires not only that the measured crater sample should be truly representative of the total population (i.e., a large sample with little or no detection efficiency "fall-off" at smaller sizes) but also that an appropriate calibration relating crater size to impactor size is available (which preferably covers the same size range as the mission data). With a new opportunity to extend the range of laboratory experiments by firing very small monodisperse projectiles within the light-gas gun (LGG), it is now possible to test whether the size of smaller particles has been correctly inferred from Al foil craters.

The crater size calibrations used in Hörz et al. (2006), relating foil crater diameter to impactor diameter, were based upon LGG shots of monodisperse soda-lime glass projectiles with diameters between approximately 10 and 100 μm. When the statistical "tail" of smaller craters (believed to be formed by projectile shards broken during the shot) was excluded, the data gave a good fit to a line with a constant gradient across the measured sizes, which, within the errors, extrapolated close to the origin, albeit with error bars of a few μm. Until very recently, this uncertainty for smaller craters could not be resolved due to a lack of suitable monodisperse projectiles of <10 μm diameter. This is unfortunate because, while the small number of large impact craters on the aluminum foils contain the majority of the captured particle mass, numerically they are far out-numbered by craters smaller than 10 μm, i.e., those made by particles in a size regime where no previous calibration was obtained directly, and whose interpretation therefore relied on extrapolation from larger events. The successful interpretation of Wild 2 cometary dust size distribution clearly requires investigation into crater size calibrations for the more numerous smaller particles.

Recent work (Kearsley et al. 2008b) has suggested that the efficiency of aluminum foil crater excavation by very small particles may be lower than for larger grains, implying that a new calibration certainly is required for this part of the size distribution. The availability of large numbers of monodisperse micrometer and smaller scale projectiles of known density, and their successful acceleration in LGG shots have proven elusive goals, only recently resolved. Accordingly, in this study we describe new calibration experiments with small particles, their preliminary results, and the implications for interpretation of particle sizes responsible for the smallest Stardust craters. We conclude by re-examining the raw data from the Stardust cometary PE, and suggest an upper limit for the subgrain sizes and their size distribution for the fundamental components of Wild 2 cometary dust aggregates.

EXPERIMENTAL METHODOLOGY

Shots were performed using the two-stage LGG at the University of Kent (Burchell et al. 1999). Projectile materials were monodisperse silica spheres commercially available from Whitehouse Scientific (UK, see http://www.whitehousescientific.com/, site accessed July 2009)

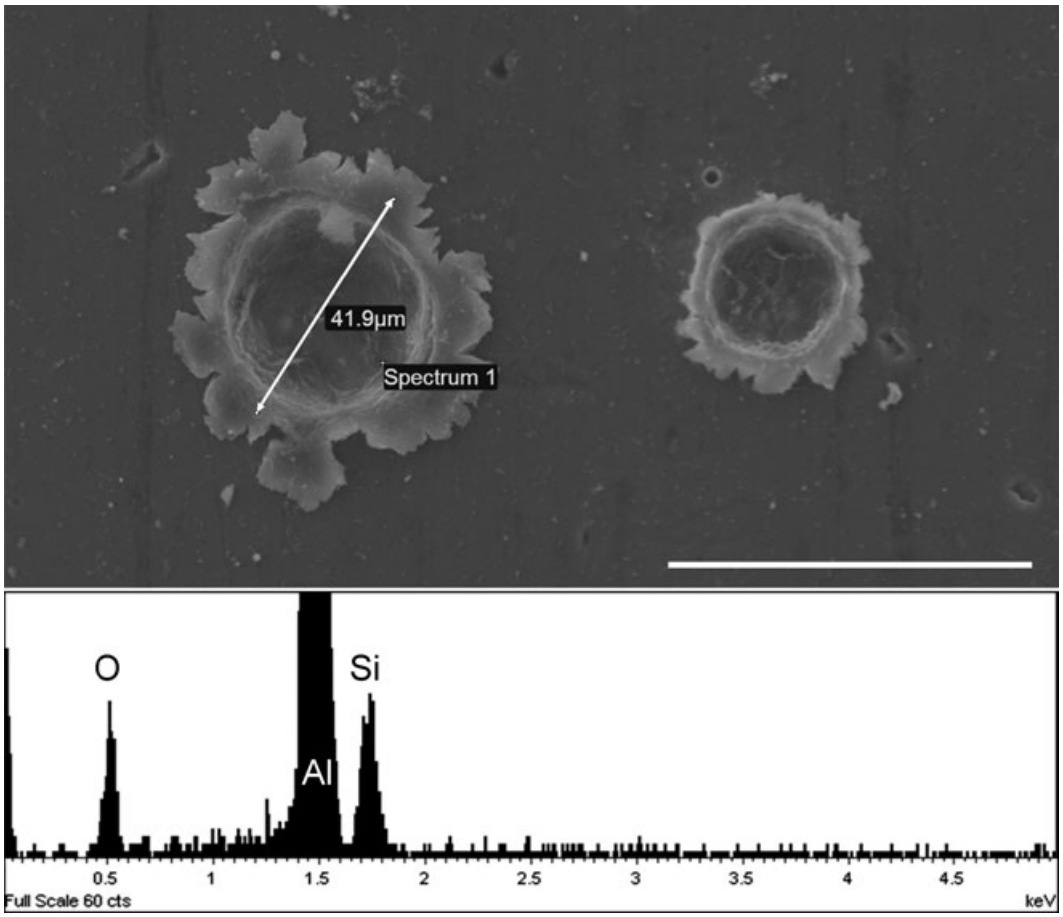

Fig. 1. Upper panel: SEM image of representative craters from silica projectile impacts showing (left) how crater top-lip to top-lip dimensions were measured; and (right) the narrower thin lip morphology. A 60 μm scale bar is shown (bottom right). Lower panel: Silicon and oxygen in a typical crater were automatically identified after a 1 s accumulation of an EDX spectrum from the crater wall, confirming an impact by a silica projectile.

and *Micromod* (Germany, see http://www.micromod.de/, site accessed July 2009). The projectiles were fired in shotgun-like blasts, with many (upwards of thousands) similar sized projectiles used in each shot. The speed in each shot was measured using a combination of sensors along the range of the gun and has a spread in each shot of order 2% around the mean speed. The velocity was calculated by measuring the time difference between exit of the sabot (containing projectiles) from the launch tube, and the impact of the sabot quadrants on the blast tank exit aperture. During each shot, the range of the gun was evacuated to approximately 0.5 mbar to prevent deceleration of the projectiles in flight. The foils used as targets were Al-1100, cut from flight spare Stardust aluminum foil, i.e., they had the same composition and thickness (~102 μm) as foils flown on Stardust (Tsou et al. 2003).

After the LGG shots, SEM imaging of the foils was carried out at the Natural History Museum (London) using a JEOL 5900 LV SEM. The size calibration of images from this instrument is routinely tested using a Richardson test slide at magnifications from 100 to 5000 times, covering the range of magnifications used in this study, and with typical errors <1% of nominal values. The identity of impactors was determined by collection of energy dispersive X-ray (EDX) spectra from each crater, to avoid potential confusion with impacts produced by gun debris (derived from sabot, burst disk, and stop-plate components, and with unconstrained grain size). Craters were measured following the method of Kearsley et al. (2006); crater diameters were defined as the distance from top of the crater lip to top of the diametrically opposed crater lip, with two measurements made for each crater to minimize error. It is, however, important to note that the measured features in small craters may not have exactly the same form as seen in larger impacts. The detachment of very thin aluminum crater lips in small craters may prevent a complete flattening out of a top lip, and hence the measured feature often has a smaller

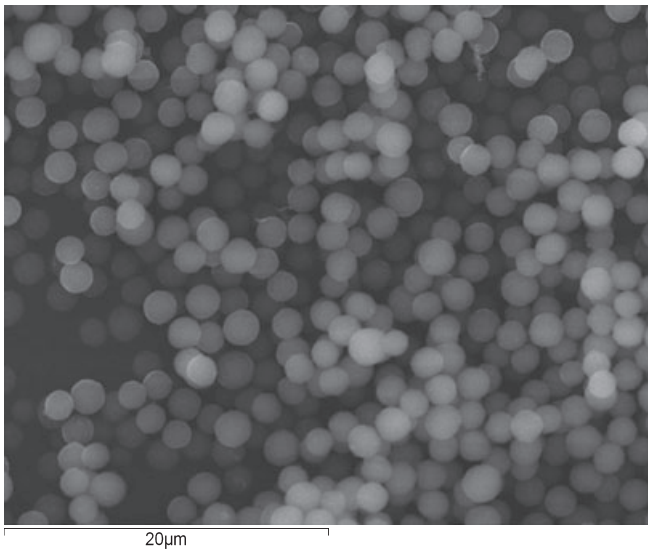

Fig. 2. Secondary electron image of (nominal) 2 μm diameter, monodisperse, silica projectiles.

diameter than expected (the ''thin lip'' of Kearsley et al. 2008b). Fortunately, the crater lip morphology seen in small experimental craters closely resembles that seen in small Stardust craters, and their direct comparison is therefore justified over the full range of sizes considered. Figure 1 shows representative craters with a measurement line highlighted, and the EDX spectrum taken from the left-hand crater, confirming that it was made by a silica impactor.

The size range of each batch of projectiles was measured in the same calibrated SEM as that used for crater measurement and analysis. For example, Fig. 2 is a SEM image of some (nominal) 2 μm diameter silica projectiles supplied by Whitehouse Scientific.

RESULTS

Nine LGG shots were carried out for this work, all at target-normal incidence (i.e., similar to that expected in the Stardust cometary encounter), and with silica projectile sizes across the size range from 0.47 to 10 μm diameter. For each shot, larger (50 μm) soda-lime glass beads were added to the contents of the sabot, to help entrain the small projectiles and launch them toward the target. The craters resulting from the impacts of these larger particles were easily identified by their large size, and were excluded from the calibration data set during analysis. However, occasionally soda-lime glass beads break up during launch, producing a wide and unconstrained size range of fragments down to very fine (submicrometer) scale. Craters arising from such fragments were particularly evident on the target foil of the smallest (0.47 μm) particle shot, where SEM–EDX spectra proved vital to ensure that only silica bead impacts were used for the size calibration.

The raw data were initially sorted in increasing value, and the highest three values and lowest three values were removed from the distribution to reduce the effects of outliers. Details of all the fit results (plus impact speeds) are given in Table 1 and details of the size distributions of the projectiles are given in Table 2. The mean speed per shot was 6.08 ± 0.15 km s^{-1}, compared to the Stardust cometary encounter speed of 6.1 km s^{-1}.

The calibration reported in Kearsley et al. (2006) was obtained in a similar fashion, but used larger soda-lime glass beads (diameter 9.8–84.2 μm). Although the two data sets may therefore seem directly comparable, as their size range just overlaps, they are based upon impactors of slightly different density and composition, and one or other has to be scaled appropriately to allow for this difference. To normalize the new data from silica (ρ_{silica} = 2.2 g cm^{-3}) to the same projectile density as the previous calibration (ρ_{soda} = 2.4 g cm^{-3}), the crater diameter (D_c) data were scaled using the experimental result given in fig. 4 of Kearsley et al. (2007). This used measurements of impact features produced by larger particles of known size but made of different materials, with densities across a range from approximately 1 to 7 g cm^{-3}, all impacted onto Stardust flight spare foils at a mean speed of approximately 6.1 km s^{-1}. Kearsley et al. (2007) suggested:

$$\frac{D_c}{D_p} = 1.9114 \ln(\rho_p) + 2.8995 \quad (1)$$

which we simplify to:

$$\frac{D_c}{D_p} = 1.91 \ln(\rho_p) + 2.90, \quad (2)$$

where ρ_p is the density of the projectile in g cm^{-3}. Thus, for direct comparability, here we adjust all silica impactor crater diameters to those predicted for impacts of the denser soda-lime glass, i.e., we multiply the measured crater diameters in Table 1 by a factor of 1.04, given simply by:

$$\left[\frac{D_c}{D_p}\right]_{sodalime} = \left(\frac{1.91 \ln 2.4 + 2.90}{1.91 \ln 2.2 + 2.90}\right) \times \left[\frac{D_c}{D_p}\right]_{silica} = 1.04 \times \left[\frac{D_c}{D_p}\right]_{silica} \quad (3)$$

Figure 3 shows projectile diameter D_p versus crater diameter D_c after density scaling, now comparable to the data from Kearsley et al. (2006) for soda-lime glass projectiles.

As can be seen in Fig. 3, at projectile diameters less than approximately 13 μm, the ratio D_c/D_p is no longer the fixed constant previously suggested by Kearsley

Table 1. Nominal (as labeled) projectile diameters, d ("m" = Micromod, "w" = Whitehouse Scientific); projectile diameters, D_p (as measured); crater diameters, D_c (before scaling); standard deviations of the distributions, σ; number of craters measured, N; number of projectiles measured, N_p (see Table 2); and the impact velocity, v, from the LGG shots.

d (μm)	$D_p \pm (\sigma/\sqrt{N_p})$ (μm)	$D_c \pm (\sigma/\sqrt{N})$ (μm)	N	v (km s^{-1}) (±2%)
0.500 (m)	0.48 ± 0.01	0.65 ± 0.06	3[a]	6.13
1.00 (m)	0.94 ± 0.01	1.64 ± 0.03	49	6.12
1.00 (w)	1.94 ± 0.01	3.00 ± 0.03	103	6.22
4.00 (w)	4.05 ± 0.03	7.86 ± 0.31	24	5.83
5.00 (w)	4.78 ± 0.01	11.39 ± 0.18	108	6.04
6.00 (w)	6.35 ± 0.04	16.63 ± 0.49	12	6.12
7.50 (w)	6.96 ± 0.05	20.36 ± 0.90	28	6.27
9.00 (w)	8.31 ± 0.07	28.22 ± 0.32	23	5.83
10.00 (w)	7.87 ± 0.10	27.86 ± 0.74[b]	91	6.12

[a]Because of their small size, it was very difficult to ascertain that all craters made in this shot arose from silica impactors and not by contaminating light-gas gun (LGG) debris or fragments of shattered soda-lime glass beads used to entrain the particles in the shot. The three craters measured here were confirmed by SEM–EDX analyses as made by silica impactors.

[b]SEM measurements of samples of the projectiles showed that their size distribution was heavily skewed (see Fig. 3) with significant numbers of larger projectiles in the (nominally) monodisperse mix. The presence of these larger projectiles during a LGG shot leads to a large scatter in the measured crater diameters.

Table 2. Mean projectile diameter, $\bar{D}_p$; median projectile diameter, $\tilde{D}_p$; number of projectiles measured, N_p; standard deviation of the distribution, σ; and number of measurements falling outside the ranges $\bar{D}_p \pm \sigma$, $\bar{D}_p \pm 3\sigma$, and $\bar{D}_p \pm 5\sigma$, respectively.

$\bar{D}_p$ (μm)	$\tilde{D}_p$ (μm)	N_p	σ (μm)	N_p [$\bar{D}_p \pm \sigma$]	N_p [$\bar{D}_p \pm 3\sigma$]	N_p [$\bar{D}_p \pm 5\sigma$]
0.48	0.48	6	0.02	1	0	0
0.94	0.94	107	0.04	35	0	0
1.94	1.93	237	0.16	74	0	0
4.04	4.05	36	0.18	12	0	0
4.80	4.78	1104	0.48	339	6	0
6.39	6.35	70	0.33	20	0	0
7.04	6.96	186	0.71	53	1	0
8.39	8.31	93	0.69	25	4	0
8.35	7.87	156	1.22	22	5	0

et al. (2006). The solid line in Fig. 3 is a spline fit to the data given by the following functions:

For $D_p < 2.4$ μm:

$$D_c = (1.60 \pm 0.17) D_p \quad (4)$$

For $2.4 < D_p < 12.7$ μm:

$$D_c = (0.91 \pm 0.11) D_p^{(1.64 \pm 0.92)} \quad (5)$$

For $D_p > 12.7$ μm:

$$D_c = (4.62 \pm 0.14) D_p \quad (6)$$

At the larger sizes, we retain the calibration factor reported by Kearsley et al. (2006); significantly, the latter was used to convert the cumulative size distributions of all Stardust craters into projectile sizes by Hörz et al. (2006). It can be seen, however, that at the smaller projectile sizes (i.e., <~13 μm diameter) the crater size decreases relative to the projectile diameter, until at the smallest sizes it is only slightly larger than the impactor. It should be noted that several repeat shots were performed to verify this observation using silica projectiles from different batches (but the same nominal diameter). Additionally, a shot was performed with polydisperse silica projectiles (with an average diameter of 20 μm) and although there was a large spread in the crater diameters measured, after density scaling, the average crater diameter fell within the error bounds of the 20 μm soda-lime glass datum. We are therefore confident that the transition to smaller crater calibration occurs within the regime described within this study, and that the previous calibration for impactors >10 μm in diameter remains valid.

We suggest that there may be two complementary mechanisms responsible for this change of cratering behavior in the aluminum.

1. It is related to the very high strain rates (~10^8 to ~10^9 s^{-1}) experienced during an impact event by very small particles. At strain rates above 10^5 s^{-1}, the yield strength of aluminum changes as a highly nonlinear function of strain rate, and increases from its quasi-static value of approximately 100 MPa to several GPa at 10^8 s^{-1}, appropriate for hypervelocity collision under Stardust encounter conditions. This strain-rate hardening is caused by the increasing lattice resistance to deformity at very high strain rates limiting the speed at which dislocations can propagate through the lattice. Price et al. (2009, 2010) performed hydrocode modeling in which the yield strength of aluminum was allowed to vary

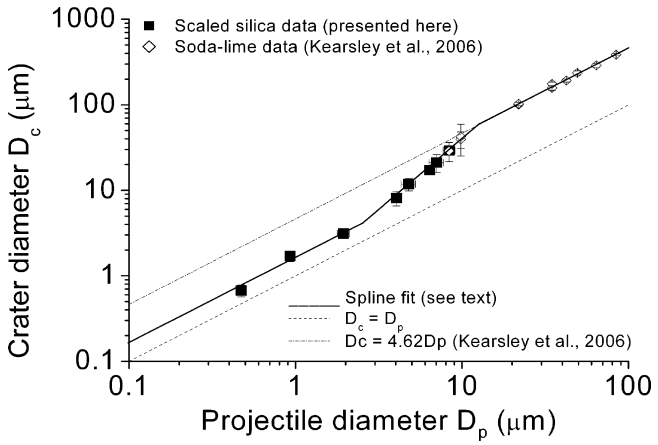

Fig. 3. Crater diameter versus projectile diameter for silica projectiles in this work (solid symbols; after density scaling) and soda-lime glass projectiles from Kearsley et al. (2006) (open symbols). A change in behavior is seen to occur for projectile diameters of between 3 and 13 μm. For $D_p < 3$ μm, the crater diameter is $1.6 \times D_p$; for $D_p > 13$ μm this ratio is 4.6, with a smooth transition at intermediate projectile diameters.

according to the experimental strain rate dependence reported in Khan and Huang (1992), Bat'kov et al. (1999), and Gilat and Cheng (2002), but capped to a maximum value of 5 GPa. The resulting modeled crater dimensions were found to fit within the spread of the experimental data presented here, giving support to the hypothesis that the change in crater excavation efficiency is a strain-rate-dependent phenomenon. Modeling has also been undertaken for impacts into high purity copper (Price et al. 2010) and tantalum (Price et al. Forthcoming) using the experimentally determined strain-rate strength dependence of those target metals and, again, the modeled crater diameters are consistent with those measured.

2. It is also probable that we are observing a change in the strength versus strain behavior of the aluminum as the projectile size decreases to become significantly smaller than the variable grain size of the Al-1100 foil (seen in electron imagery, e.g., Kearsley et al. 2006, fig. 4, to be as small as a few tens of micrometers in places). For large impactors (with diameters larger than the local target grain size), the effective yield strength of the Al is that of the bulk material, with potential for deformation along weak intercrystalline boundaries becoming important. However, as the projectile decreases in size to the point that it is very much smaller (<1 μm) than the local Al grain size, statistically it will be more likely to impact away from the edge on a single crystal, where the strength is dominated by the (much stronger) crystal lattice, and controlled by the crystallographic orientation. We might therefore expect more variable crater diameters and depth profiles as a result, although crater plan-view surface asymmetry is unlikely, and measurement of a depth profile by the techniques of Kearsley et al. (2008b) is unlikely to be successful for such small craters. The effect of grain size and crystallographic orientation on the strength of aluminum is discussed extensively in Komanduri et al. (2000), Sun et al. (2006), and Farrokh and Khan (2009). However, because Stardust foil surfaces present only a planar section through complex 3-D, polygonal crystal shapes (flattened by rolling during foil fabrication) it is also not possible for us to make a simple judgement as to the proximity of a particular crater to all possibly significant grain boundaries (which may lie beneath). So far, we have found no evidence of a wider range of crater morphology in our smallest (~500 nm) impactor shots; this is in contrast to the wide range of shape seen in the smaller Stardust craters (see below) which we have attributed to complex internal structures with Wild 2 dust grains (Kearsley et al. 2009).

Further interpretation of the physical basis for small crater growth might be aided by a program of shots onto coarse, single-crystal aluminum targets, and mesoscale hydrocode modeling (i.e., implicitly modeling the random crystal orientations within the aluminum foil), to resolve which processes dominate.

DISCUSSION

Even when applied without any further correction, e.g., for the diverse nature of individual impactors, our new calibration has a significant effect on an estimate of cumulative dust particle fluence at small sizes. By comparison to the previous estimates, the diameters of the smaller dust grains should now be increased by a factor of 2.9, implying an increase by a factor of approximately 24 in their volume and mass (but see discussion of mass implications below). To show how this influences the Stardust results for dust particle size from comet 81P/Wild 2, we revisit the crater size distribution data originally presented in Hörz et al. (2006). The crater data in Hörz et al. (2006) were divided into two sets: a set of 281 small (<20 μm diameter) craters observed in SEM studies of foils C2008N, C2020W, C2037N, and C2052N (for a map of the foil locations see Kearsley et al. 2008a); and a second set of 63 large (>20 μm diameter) craters, obtained by optical scanning of all the foils on the entire collector tray. Normalizing the cumulative data

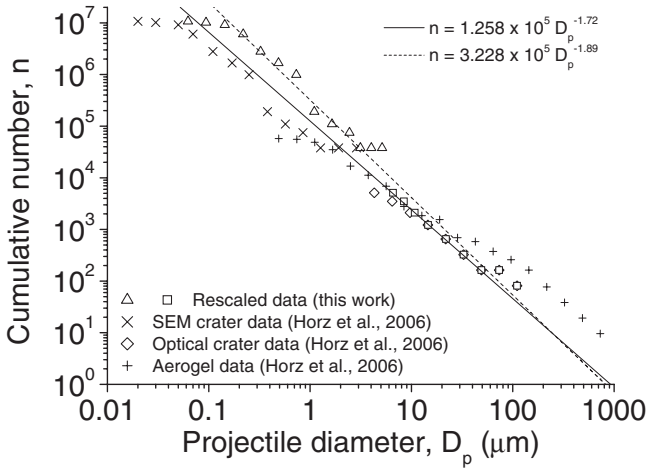

Fig. 4. Cumulative cometary dust particle size distribution obtained for 81P/Wild 2 from measurements of craters in Al foil on the Stardust. Note that the two sets of results (Hörz et al. 2006; and the new results presented here) are based on the same data set of crater measurements; the change at small particle sizes is due to the new calibration. Two fit curves are shown, the solid line is from the original report in Hörz et al. (2006) and the dashed line is the new fit to the crater data. The flattening of the data seen for the aerogel data (at $D_p \sim 1$ μm) and the crater data (at $D_p \sim 0.05$ μm) is indicative of a fall-off in detection efficiency at these very small scales.

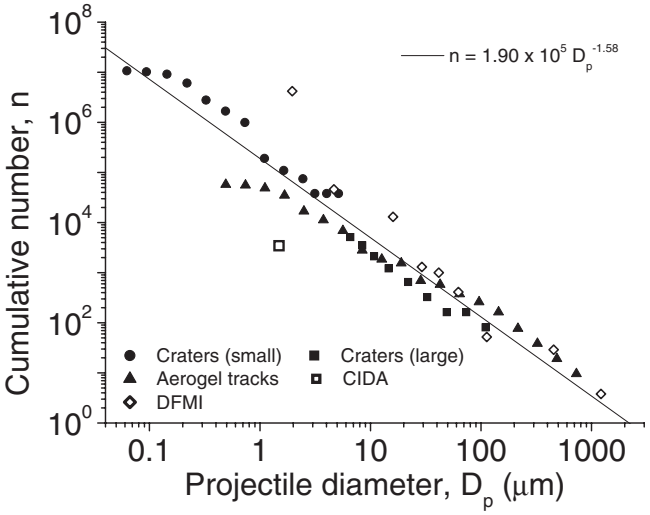

Fig. 5. Stardust cumulative dust flux curve for 81P/Wild 2. Shown are the results of postflight measurements made with the different data sets: craters in aluminum, tracks in aerogel. A single fit was made to the entire data set (craters and tracks) and is shown as a solid line. Also shown are the data taken during encounter from the CIDA and DFMI instruments.

to the appropriate collector areas produced a measure of the cumulative number of dust grains per m^2 intercepted by the Stardust spacecraft (fig. 4 in Hörz et al. 2006). Although we are not presenting new data on crater numbers, the implied impactor size interpretation now needs to be adjusted for the effects of the new calibration.

Figure 4 shows the newly obtained cumulative size distribution, compared with that given in Hörz et al. (2006) (analyzed with the original calibration of Kearsley et al. 2006). Power law fits show that the index of the cumulative size distribution changes from its previous value of −1.72 (Hörz et al. 2006) to −1.89, indicating that a larger mass fraction is contained within smaller projectiles than previously assumed.

When the rescaled crater data are plotted (Fig. 5) with the other Stardust dust flux distribution data sets (i.e., the aerogel track results and the measurements made during the cometary encounter by DFMI and CIDA, originally presented as fig. 4 in Hörz et al. 2006), a single power law fit made to the crater and aerogel data over the dust grain size range 0.1–1000 μm has a slope of $1.58 \pm \frac{0.023}{0.130}$, where the uncertainty range has been estimated by taking the minimum and maximum slope of a line that just passes through two data points in the data set.

The substantial revision of size for smaller impacting particles, apparent from the new calibration, also has implications for the distribution of mass. If mass within size intervals is calculated for the line equations shown in the fluence plot of Fig. 4 ($1.258 \times 10^5 \ D_p^{-1.72}$ for the older calibration, and $3.228 \times 10^5 \ D_p^{-1.89}$ for the revised calibration), an increase is seen for smaller sizes (Fig. 6), but only very modest (from ~3% to ~5% for particles <50 μm in diameter). For particles <10 μm in diameter, the increase is from 0.4% to 0.8% of the total, and the conclusion of Kearsley et al. (2008a) that such particles comprise a small proportion of the total cometary dust mass remains valid. Evidence from crater depth profiles (Kearsley et al. 2008a, 2008b, 2009) also indicates that the density of most of the larger particles was relatively high, and they should not be considered as highly porous, of low density, and hence low mass contributors. Indeed, Fig. 5 shows that the number of the very largest impacts exceeds the best-fit simple line plot, implying that an even greater proportion of mass lies in the biggest impactors.

WILD 2 DUST SIZE: IMPACTOR COMPOSITION, STRUCTURE, AND CONSTITUENT SUBGRAINS

When interpreting a size distribution such as that shown in Fig. 4, it is important to consider the influence of the sampling and measurement method, its relationship to the pristine particle structure, and the

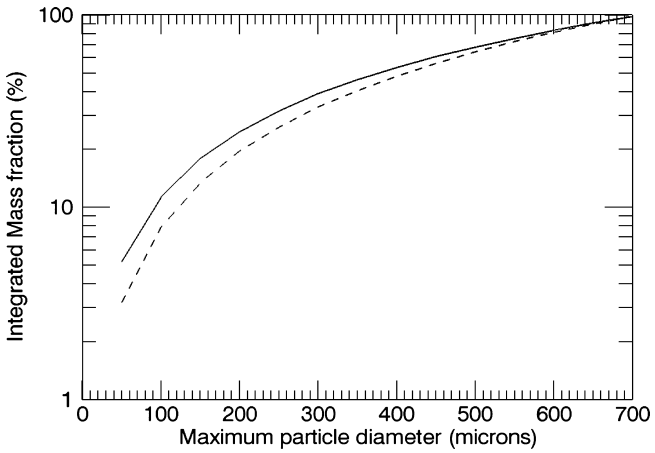

Fig. 6. Mass contribution to the total Stardust collection for 81P/Wild 2 grains. Older calibration (dashed line), revised calibration (this study, solid line).

potential role of dynamic evolution of dust in the coma. Calibration work has clearly shown that dimensions of aerogel tracks and aluminum craters can be used as proxies for impacting particle overall size. However, we must not equate this type of "ISD" with the fundamental size distribution (FSD) of the smaller solid (silicate- and sulfide-dominated) particle components that we might observe, aggregated with ice or organic material, on a cometary nucleus, prior to dust ejection and disaggregation. There is now abundant evidence of fragmentation of cometary particles following their release from the nucleus and passage through the coma (Weissman and Lowry 2008). Mass distribution as measured by a spacecraft passing through the coma will therefore differ from that at the surface of the comet nucleus. The higher ejection velocity of smaller particles gives a shorter duration of transit prior to collection (see McDonnell et al. 1991 for further discussion of how this influenced Giotto data from comet Halley) and hence less time for modification, although their greater ratio of external surface area to volume may enhance disaggregation. The rapid bursts of particle impacts recorded by DFMI during the coma transit (Green et al. 2004) suggest that what we now see captured in aerogel and on Al foil is a series of superimposed snapshots of the localized evolutionary state of the dust. Supporting this is evidence of clustering in the impacts on the Stardust foils and aerogel (Burchell et al. 2008; Westphal et al. 2008). Were we to sample the same constituent material at times before and after the actual collection, it is probable that we would see different grain size distributions, neither fully matching the FSD. This is particularly likely if much of the released coarser dust was composed of weakly bound aggregates (as suggested by Kearsley et al. 2009) which may continue to disintegrate with time (Weissman and Lowry 2008; Westphal et al. 2008). So, to understand the processes responsible for the initial accretion of the cometary dust, rather than just the mechanism of its eventual break up, we should try to measure the size of the discrete fundamental components, as well as that of their aggregates. The true size distribution (FSD) of the individual dust components is therefore certain to be smaller than indicated by our Fig. 4. Similarly, the fundamental mass distribution within specific size fractions cannot be calculated directly from the "raw" ISD fluence plot, but requires additional knowledge of subgrain dimensions and compositions within aggregates.

Indeed, although the plan-view lateral dimensions of a crater may be a fair proxy for the overall impactor size, without information from a crater's 3-D morphology (Kearsley et al. 2009), it is not possible to derive directly particle mass unless the internal particle structure (and hence impactor density) is known. Thus, calculations derived from crater diameter alone must be regarded as giving a relatively crude estimation of particle mass, as the experimental calibration is necessarily based upon impactors which are spherical, relatively dense, nonporous particles that may not closely resemble even the majority of cometary aggregate dust grains. The simple conversion of particle diameters to masses for different density values (as shown on the *X*-axis in fig. 4 of Hörz et al. 2006) thus gives maximum values. Subgrain separation (pore space) within an impactor can yield a lower overall mass at constant diameter, yet still be responsible for a relatively broad (albeit shallow) crater.

It is therefore important to determine whether individual dust grains were single component dense impactors or porous aggregates. This may sometimes be apparent from the presence of overlapping bowls giving rise to compound craters. Indeed, where SEM images are available (e.g., Fig. 7) it is clear that many of the smaller Stardust craters seen in PE were irregular, probably formed by aggregate particles (Kearsley et al. 2009).

However, very recent molecular dynamics simulations of impacts by 50 nm scale grains also suggest that the local orientation of the crystal lattice in the impacted target may influence the shape of the resulting crater for the very smallest impactors (Park, unpublished work). Metal-on-metal impacts studied by molecular dynamics show that the crystal orientation of the underlying metal target has an effect on the observed crater morphology. This effect is particularly noticeable when the crater is viewed from above, as is the case with SEM observations. Where the target crystal is oriented such that the high-symmetry directions (<100>, <110>, <111>) are normal to the

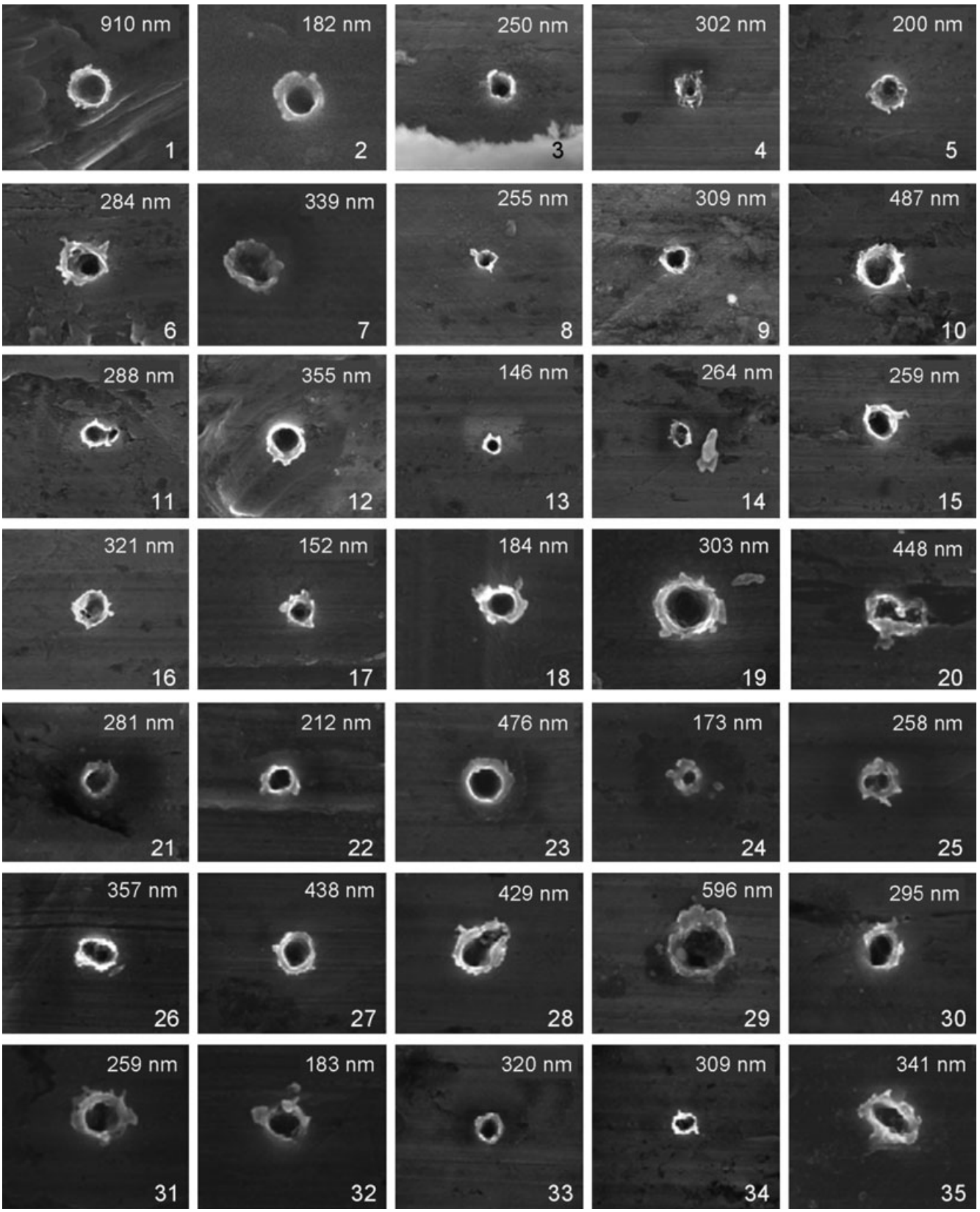

Fig. 7. Representative small Stardust foil craters found on foil C2100N,1 (see Table A12). Dimension (top right of each image) refers to averaged crater diameter as calculated by the investigator.

surface, and hence parallel to the direction of impact, the initial distortion observed strongly reflects the underlying structure. However, later morphology indicates a more circular bowl, and the expelled lip material cracks and breaks off such that the lattice orientation is no longer obvious. Lower symmetry orientations, on the other hand, show less distinct noncircular early time behavior. However, in this case the bowl shape persists to later times, and the lip cracks are less uniformly spread around the bowl circumference. The bowl interior shape, as with the top-lip circumference, shows differences between high-symmetry and low-symmetry orientation. In the high-symmetry case, the bowl is smoothly curved in all directions. Here, the bowl interior surface is coated by the molten projectile material. In the low-symmetry case, the bowl sides show flattened regions, and although the bowl sides are coated with the molten residue from the projectile, this coating is nonuniform in thickness.

Widely differing sizes and orientations of individual crystals in the Al foil are apparent in high-contrast backscattered electron images, and it is therefore not possible to make a simple correction for this factor. Unfortunately, if the component subgrains of an aggregate are each very small relative to the overall aggregate size, the overall crater morphology can also assume a simple bowl shape (Kearsley et al. 2009). Only when a 3-D reconstruction of the bowl-shaped crater can be made is it possible to confirm a relatively shallow depth profile, indicative of either a low-density impactor (i.e., with multiple smaller dense grains in a porous aggregate structure), or a homogenous low-density impactor. Acquisition of such digital elevation maps of craters is a very time-consuming process, especially for submicrometer craters, and was impractical for large numbers examined during the very short PE phase. However, for future investigations, it is recommended that all craters be documented with carefully aligned stereopair images.

Another important clue to particle internal structure can be found in analyses of residues in the crater. The complexity of interpretation of EDX spectra from within complex topographic surfaces is described in Kearsley et al. (2006), who concluded that quantification of in situ analyses from within unprepared small craters is not possible; although in some cases mineral species can be identified (e.g., see Wozniakiewicz et al. 2009), and FIB sections of small craters have subsequently yielded excellent analytical TEM data (e.g., Graham et al. 2006; Leroux et al. 2008). Nevertheless, even a small list of elements detected within a crater by SEM–EDX can suggest whether single or multiple compositional components were present in the impactor. This may reveal whether the particle was an aggregate of some kind, even when no further information about internal structure and textural relationships can be obtained. During PE, X-ray spectra were taken from only a limited number of craters, and with differing analytical instruments and protocols. Direct comparability is therefore difficult, and a complete synthesis cannot be made from the limited number of analyzed craters. Nevertheless, an important trend becomes apparent. The classification of small crater residues in Kearsley et al. (2008a) shows that a substantial proportion contained indications of both mafic silicate (Mg and Si detected) and sulfide (S detected) components within a single impactor. FIB-TEM studies by Leroux et al. (2008) have even shown that discrete sulfide and silicate components may survive as separate melt-patches or mineral-fragments, although the craters may not clearly show the original grain size and interrelationships of each component. In this study, we have returned to the original PE records and where compositional information is available for a specific crater, we have attempted to apply a simple classification (see Table A1), reflecting whether one or more components were present in a particular impactor. For example: if only Mg and Si are detected (with or without Ca and Fe), the impactor has been classified as mafic silicate "m"; if only Fe and S were detected (with or without Ni), the particle was classified as sulfide "su." A combination of Mg, Si, S, and Fe is regarded as composed of two discrete components "m and su," rather than their direct incorporation into a single mineral phase (e.g., a mixed phyllosilicate and oxy-sulfide such as that occurring in type 1 and 2 carbonaceous chondrite meteorites, but which has not yet been reported from any Wild 2 samples). However, we cannot exclude the possibility of silicate and sulfide coexistence in an amorphous mixture (e.g., GEMS of Bradley et al. 1999), although such material has not yet been unambiguously identified from Stardust materials (either on foil or aerogel; Ishii et al. 2008). From this classification of craters by contained impact residues, we can draw two useful results to aid calibration (1) whether an individual particle should be regarded as composed of one or at least two subgrains and (2) a sensible density-scaling factor that can be applied to correct the particle size calibration for that individual impactor.

For each crater where there is EDX evidence of multiple compositional components, we have made a simple assumption: that it was made by an equal pair of fundamental subgrains, one silicate, the other being sulfide. We know that this cannot be an accurate reflection of the true aggregate make-up, as there is wide variation in the ratios of the EDX peak integrals

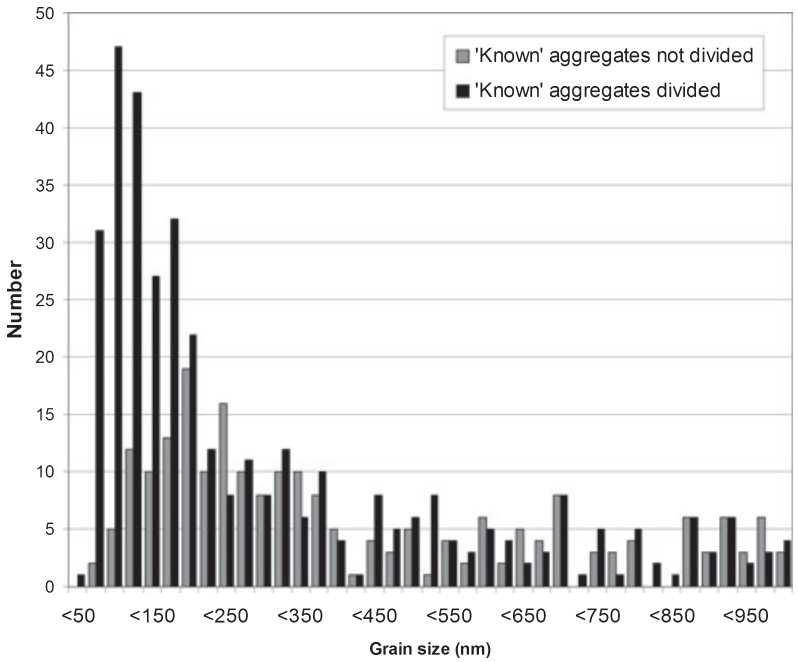

Fig. 8. Comparison of particle size abundance measurements determined from systematic surveys of Stardust Al foils for smaller (sub-μm) craters. Note that the mode is at a smaller size when more than one particle is counted for craters suspected to be from aggregate particles. The true "fundamental" size mode is likely to be at an even smaller size, as aggregates have been interpreted as containing only two subgrains. Also, the morphology and composition of residues were only determinable for 36% of the total data set (see text), and hence the number of aggregates will be substantially higher, again shifting the mode still further to the left.

between spectra, which implies that the modal proportions of fundamental compositional components vary a great deal. Nevertheless, although it is not possible to make an accurate quantitative measurement, the division into subgrain components must give us a better model for grain size than assuming a single grain structure, even if only by boosting the numbers of smaller grains counted in the FSD. Similarly, where we can show that a crater has a compound morphology, we have again assumed it to have been made by two fundamental subgrains held together in an aggregate. Usually, we do not have compositional information as well as crater morphology, and so we treat the impactor as likely to be dominated by mafic silicate. To measure the size of the fundamental subgrains within aggregates we employ the new calibration scaled to reflect a bulk grain density of 2.4 g cm^{-3}, as suggested for larger aggregates by Kearsley et al. (2009), and implying some internal pore space in the aggregate. The determined impactor volume is then divided into two halves, each of which is recast as a separate fundamental particle, whose diameter and mass are calculated (with a density correction if appropriate). The two fundamental particles are then added to the size and mass distribution data set, in place of the single aggregate value. When this process was completed for all of the craters for which PE had yielded compositional or morphological information (see Tables A2–A13), the particle size distribution in Fig. 8 was obtained.

It is important to realize that the division of aggregates into fundamental particles in this data set is far from complete. We have only been able to suggest aggregate structure for those craters where EDX or morphological data are available (206 of 572 craters, ~36%). Larger Wild 2 dust grains examined by TEM (e.g., Brownlee et al. 2006) and synchrotron X-ray computed tomography (Nakamura et al. 2008) have shown that multiple mafic silicate phases may be present, tightly packed together within a single impactor. The very fine scale mixing of crater residues, and coarse analytical sampling volume of in situ EDX, mean that we cannot recognize these complex grains. It is also very unlikely that most aggregates are made of just two fundamental grains, or that both are of equal size. Hence, our simple assumptions cannot possibly fully reflect the true variation in subgrain numbers, size, and proportion of composition that occurs in Wild 2 dust aggregates, but they do give a better evaluation of the maximum fundamental particle size than raw crater data alone. With systematic surveys of large Stardust foil areas now being carried out at very high resolution, the record of submicrometer craters will undoubtedly

improve. In future, it should be possible to evaluate numbers of smaller craters than imaged during PE, almost certainly shifting our apparent mode for the most abundant grain components to an even smaller size.

CONCLUSIONS, IMPLICATIONS, AND FUTURE WORK

New experimental data extend the calibration of crater size on the Stardust aluminum foils to submicrometer-sized impactors. The ratio of crater to projectile diameter was found to be significantly different for projectile diameters of <13 μm. At the larger sizes, the calibration of Kearsley et al. (2006) still holds, but a new and more appropriate calibration is suggested for the smaller projectiles. In earlier studies, the diameter of the smaller dust particles was therefore underestimated by a factor of approximately 2.9 and hence their mass was underestimated by a factor of approximately 24. Our new work with small projectiles also has implications for further interpretation of the density in impactors responsible for compound craters seen on Stardust foils. To extend and refine the calibration still further, even smaller (0.1 μm diameter) silica spheres have now been obtained and fired at foil, the measurement of their submicrometer crater dimensions requires high-resolution field emission SEM, and has now begun. Repeat shots of the larger projectile sizes will also be performed to further improve measurement statistics. Our aim is to extend calibration to cover the entire range of Stardust foil crater sizes.

The revised calibration has several important implications. For example, when analyzing small Stardust craters (crater diameter <3 μm), Leroux et al. (2008) obtained an estimate of the volume of impactor residue retained in the crater. This was compared to the volume of impactor, inferred from the crater diameter, using the calibration of Kearsley et al. (2006, 2007). They found near equivalence of the two quantities, and concluded that the majority of the impactor was retained as residue in the crater. With the new calibration we can now see that this is not the case, and the preserved mass would now be estimated as only approximately 5% of that of the impactor. Our recent experimental evidence suggests that this is a substantially lower proportion of the projectile than is preserved in impacts of grains >10 μm in diameter, and may reflect the greater partitioning of damage into the impactor as the strain rate increases. Greater impact-driven modification to smaller sized projectiles has also been suggested to account for their more extreme volatile depletion (e.g., pyrrhotite sulfur loss; Kearsley et al. 2007).

We have also used the new calibration to revise our measure of the cumulative dust fluence of the comet 81P/Wild 2 encounter. Notably, the cumulative fluence data for dust particles of ≥3 μm diameter are now comparable between the returned collector (craters and aerogel) and the encounter data from DFMI. There is, however, still a substantial discrepancy for smaller (1 μm) dust particles, with the measurements made during encounter by CIDA and DFMI bracketing the results from the returned sample analysis. We also find that the mode size of 81P/Wild 2 dust grains intercepted by the Stardust spacecraft was approximately 175 nm or less, but that if allowance is made for a possible aggregate-like structure of the grains, the component subgrain size distribution almost certainly has a mode size of <100 nm.

The results from 81P/Wild 2 have been compared to other comets (see Hörz et al. 2006; Burchell et al. 2008). The slope of the size distribution was originally reported as −1.72, i.e., intermediate between that for 26P/Grigg–Skjellerup (−0.93; McDonnell et al. 1993) and that of 1P/Halley (−2.6 ± 0.2; McDonnell et al. 1991; Fulle et al. 2000); see Burchell et al. (2008) for a discussion. The updated slope found here (−1.89) is slightly closer than before to that of 1P/Halley but not sufficiently to classify it as the same type.

Acknowledgments—The work at the University of Kent was funded by a grant from the STFC (UK). H. L. and J. B. thank the CNES (Centre National des Etudes Spatiales) for their support. Contributions from N. T. and P. J. W. were performed under the auspices of the USA. DoE by LLNL under contract DE-AC52-07NA27344.

Editorial Handling—Dr. Scott Sandford

REFERENCES

Bat'kov Y. V., Knyazev V. N., Novikov S. A., Rayevskii V. A., and Fishman N. D. 1999. Shear strength of aluminum upon shockless compression. *Combustion, Explosion and Shockwaves* 35:115–118.

Bradley J. P., Keller L. P., Snow T. P., Hanner M. S., Flynn G. J., Gezo J. C., Clemett S. J., Brownlee D. E., and Bowey J. E. 1999. An infrared spectral match between GEMS and interstellar grains. *Science* 285:1716–1718.

Brownlee D. E., Tsou P., Aléon J., Alexander C. M. O'D., Araki T., Bajt S., Baratta G. A., Bastien R., Bland P., Bleuet P., Borg J., Bradley J. P., Brearley A., Brenker F., Brennan S., Bridges J. C., Browning N., Brucato J. R., Brucato H., Bullock E., Burchell M. J., Busemann H., Butterworth A., Chaussidon M., Cheuvront A., Chi M., Cintala M. J., Clark B. C., Clemett S. J., Cody G., Colangeli L., Cooper G., Cordier P. G., Daghlian C., Dai Z., D'Hendecourt L., Djouadi Z., Dominguez G., Duxbury T., Dworkin J. P., Ebel D., Economou T. E., Fairey S. A.

J., Fallon S., Ferrini G., Ferroir T., Fleckenstein H., Floss C., Flynn G., Franchi I. A., Fries M., Gainsforth Z., Gallien J.-P., Genge M., Gilles M. K., Gillet P., Gilmour J., Glavin D. P., Gounelle M., Grady M. M., Graham G. A., Grant P. G., Green S. F., Grossemy F., Grossman L., Grossman J., Guan Y., Hagiya K., Harvey R., Heck P., Herzog G. F., Hoppe P., Hörz F., Huth J., Hutcheon I. D., Ishii H., Ito M., Jacob D., Jacobsen C., Jacobsen S., Joswiak D., Kearsley A. T., Keller L., Khodja H., Kilcoyne A. L. D., Kissel J., Krot A., Langenhorst F., Lanzirotti A., Le L., Leshin L., Leitner J., Lemelle L., Leroux H., Liu M.-C., Luening K., Lyon I., MacPherson G., Marcus M. A., Marhas K., Matrajt G., Meibom A., Mennella V., Messenger K., Mikouchi T., Mostefaoui S., Nakamura T., Nakano T., Newville M., Nittler L. R., Ohnishi I., Ohsumi K., Okudaira K., Papanastassiou D. A., Palma R., Palumbo M. O., Pepin R. E., Perkins D., Perronnet M., Pianetta P., Rao W., Rietmeijer F., Robert F., Rost D., Rotundi A., Ryan R., Sandford S. A., Schwandt C. S., See T. H., Schlutter D., Sheffield-Parker J. A., Simionovici S., Sitnitsky S. I., Snead C. J., Spencer M. K., Stadermann F. J., Steele A., Stephan T., Stroud R., Susini J., Sutton S. R., Taheri M., Taylor S., Teslich N., Tomeoka K., Tomioka N., Toppani A., Trigo-Rodríguez J. M., Troadec D., Tsuchiyama A., Tuzolino A. J., Tyliszczak T., Uesugi K., Velbel M., Vellenga J., Vicenzi E., Vincze L., Warren J., Weber I., Weisberg M., Westphal A. J., Wirick S., Wooden D., Wopenka B., Wozniakiewicz P. A., Wright I., Yabuta H., Yano H., Young E. D., Zare R. N., Zega T., Ziegler K., Zimmerman L., Zinner E., and Zolensky M. 2006. Comet 81P/Wild 2 under a microscope. *Science* 314:1711–1716.

Burchell M. J., Cole M. J., McDonnell J. A. M., and Zarnecki J. C. 1999. Hypervelocity impact studies using the 2 MV Van de Graaff accelerator and two-stage light gas gun of the University of Kent at Canterbury. *Measurement Science Technology* 10:41–50.

Burchell M. J., Fairey S. A. J., Wozniakiewicz P., Brownlee D. E., Hörz F., Kearsley A. T., See T. H., Tsou P., Westphal A., Green S. F., Trigo-Rodríguez J. M., and Domingúez G. 2008. Characteristics of cometary dust tracks in Stardust aerogel and laboratory calibrations. *Meteoritics & Planetary Science* 43:23–40.

Farrokh B. and Khan A. S. 2009. Grain size, strain rate and temperature dependence of flow stress in ultra-fine grained and nanocrystalline Cu and Al: Synthesis, experiment and constitutive modeling. *International Journal of Plasticity* 25:715–732.

Fulle M., Levasseur-Regourd A. C., McBride N., and Hadamcik N. 2000. In-situ dust measurements from within the coma of 1P/Halley: First order approximation with a dynamical dust model. *The Astronomical Journal* 119:1968–1977.

Gilat A. and Cheng C. 2002. Modeling torsional split Hopkinson bar tests at strain rates above 10,000 s^{-1}. *International Journal of Plasticity* 18:787–799.

Graham G. A., Teslich N., Dai Z., Bradley J. P., Kearsley A. T., and Hörz F. P. 2006. Focused ion beam recovery of hypervelocity impact residue in experimental craters on metallic foils. *Meteoritics & Planetary Science* 41:159–165.

Green S. F., McDonnell J. A. M., McBride N., Colwell M. T. S. H., Tuzzolino A. J., Economou T. E., Tsou P., Clark B. C., and Brownlee D. E. 2004. The dust mass distribution of comet 81P/Wild 2. *Journal of Geophysical Research* 109, doi:10.1029/2004JE002318.

Hanner M. S. and Bradley J. P. 2004. Composition and mineralogy of cometary dust. In *Comets II*, edited by Festou M. C., Keller H. U., and Weaver H. A. Tucson, AZ: The University of Arizona Press. pp. 555–564.

Hörz F., Bastien R., Borg J., Bradley J. P., Bridges J. C., Brownlee D. E., Burchell M. J., Cintala M. J., Dai Z. R., Djouadi Z., Dominguez G., Economou T. E., Fairey S. A. J., Floss C., Franchi I. A., Graham G. A., Green S. F., Heck H., Hoppe P., Huth J., Ishii H., Kearsley A. T., Kissel J., Leitner J., Leroux H., Marhas M., Messenger K., Schwandt C. S., See T. H., Snead S., Stadermann F. J., Stephan T., Stroud R., Teslich N., Trigo-Rodríguez J. M., Tuzzolino A. J., Troadec D., Tsou P., Warren J., Westphal A., Wozniakiewicz P. J., Wright I., and Zinner E. 2006. Impact features on Stardust: Implications for comet 81P/Wild 2 dust. *Science* 314:1716–1719.

Ishii H., Bradley J. P., Dai Z. R., Chi M., Kearsley A. T., Burchell M. J., Browning N. D., and Molster F. J. 2008. Comparison of 81P/Wild 2 dust with interplanetary dust from comets. *Science* 319:447–450.

Kearsley A. T., Burchell M. J., Hörz F., Cole M. J., and Schwandt C. S. 2006. Laboratory simulations of impacts upon aluminum foils of the Stardust spacecraft: Calibration of dust particle size from comet Wild 2. *Meteoritics & Planetary Science* 41:167–180.

Kearsley A. T., Graham G. A., Burchell M. J., Cole M. J., Dai Z., Teslich N., Chater R. J., Wozniakiewicz P. J., Spratt J., and Jones G. 2007. Analytical scanning and transmission electron microscopy of laboratory impacts on Stardust aluminum foils: Interpreting impact crater morphology and the composition of impact residues. *Meteoritics & Planetary Science* 42:191–210.

Kearsley A. T., Borg J., Graham G. A., Burchell M. J., Cole M. J., Leroux H., Bridges J. C., Hörz F., Wozniakiewicz P. J., Bland P. A., Bradley J. P., Dai Z. R., Teslich N., See T., Hoppe P., Heck P. R., Huth J., Stadermann F. J., Floss C., Marhas K., Stephan T., and Leitner J. 2008a. Dust from comet Wild 2: Interpreting particle size, shape, structure and composition from impact features on the Stardust aluminum foils. *Meteoritics & Planetary Science* 43:41–74.

Kearsley A. T., Graham G. A., Burchell M. J., Cole M. J., Wozniakiewicz P. J., Teslich N., Bringa E., Hörz F., Blüm P., and Poppe T. 2008b. Micro-craters in aluminum foils on NASA's Stardust spacecraft: Implications for dust microparticles emanating from comet Wild 2. *International Journal of Impact Engineering* 35:1616–1624.

Kearsley A. T., Burchell M. J., Price M. C., Graham G. A., Wozniakiewicz P. J., Cole M. J., Foster N. J., and Teslich N. 2009. Interpretation of Wild 2 dust fine structure: Comparison of Stardust aluminum foil craters to three dimensional shape of experimental impacts by artificial aggregate particles and meteorite powders. *Meteoritics & Planetary Science* 44:1489–1510.

Khan A. S. and Huang S. 1992. Experimental and theoretical study of mechanical behavior of 1100 aluminum in the strain rate range 10^{-5} – 10^{4} s^{-1}. *International Journal of Plasticity* 8:397–424.

Kissel J., Krueger F. R., Silén J., and Clark B. C. 2004. The cometary and interstellar dust analyzer at comet 81P/Wild 2. *Science* 304:1774–1776.

Komanduri R., Chandrasekeran N., and Raff L. M. 2000. MD simulation of indentation and scratching of single crystal aluminum. *Wear* 240:113–143.

Leroux H., Stroud R. M., Dai Z. R., Graham G. A., Troadec D., Bradley J. P., Teslich N., Borg J., Kearsley A. T., and Hörz F. 2008. Transmission electron microscopy of cometary residues from micron-sized craters in the Stardust Al foils. *Meteoritics & Planetary Science* 43:143–160.

Levasseur-Regourd A. C., Mukai T., Lasue J., and Okada Y. 2007. Physical properties of cometary and interplanetary dust. *Planetary and Space Science* 55:1010–1020.

McDonnell J. A. M., Alexander W. M., Burton W. M., Bussoletti E., Evans G. C., Evans S. T., Firth J. G., Grard R. J. L., Green S. F., Grün E., Hanner M. S., Hughes D. W., Igenburgs E., Kissel J., Kuczera H., Lindblad B. A., Langevin Y., Mandeville J. C., Nappo S., Pankiewicz G. S. A., Perry C. H., Schwehm G. H., Sekanina Z., Stevenson T. J., Turner R. F., Weishaupt U., Wallis M. K., and Zarnecki J. C. 1987. The dust distribution within the inner coma of comet P/Halley 1982i: Encounter by Giotto's impact detectors. *Astronomy & Astrophysics* 187:719–741.

McDonnell J. A. M., Lamy P. L., and Pankiewicz G. S. 1991. Physical properties of cometary dust. In *Comets in the post-Halley era*, vol. 2, edited by Newburn R. L. Jr., Neugebauer M., and Rahe J. Norwell, MA: Kluwer Academic. pp. 1043–1073.

McDonnell J. A. M., McBride N., Beard R., Bussoletti E., Colangeli L., Eberhardt P., Firth J. G., Grard R., Green S. F., Greenberg J. M., Grun E., Hughes D. W., Keller H. U., Kissel J., Lindblad B. A., Mandeville J. C., Perry C. H., Rembor K., Rickman H., Schwehm G. H., Turner R. F., Wallis M. K., and Zarnecki J. C. 1993. Dust particle impacts during the Giotto encounter with comet Grigg-Skjellerup. *Nature* 362:732–734.

Nakamura T., Noguchi T., Tsuchiyama A., Ushikubo T., Kita N. T., Valley J. W., Zolensky M. E., Kakazu Y., Sakamoto K., Mashio E., Uesugi K., and Nakano K., 2008. Mineralogy, three dimensional structure, and oxygen isotope ratios of four crystalline particles from comet 81P/Wild 2 (abstract #1695). 39th Lunar and Planetary Science Conference. CD-ROM.

Price M. C., Kearsley A. T., and Burchell M. J. 2009. *Stardust* cometary and interstellar dust collector calibration: Modelling impacts on Al-1100 foil at velocities up to 20 km s^{-1} and comparison with experimental data Proceedings of the European Planetary Science Congress, Potsdam, 2009. Vol. 4, abstract #EPSC2009-600-1.

Price M. C., Kearsley A. T., and Burchell M. J. 2010. Using hypervelocity impact crater morphologies to validate the ultra-high strain rate strength of target metals: Al-1100 and high purity copper. Proceedings of the 11th Hypervelocity Impact Symposium, Frieburg, 2010. Article #A38.

Price M. C., Kearsley A. T., and Burchell M. J. Forthcoming. Ultra high strain rate yield strengths of Al, Cu, Nb and Ta: Insights from hypervelocity impacts and hydrocode modelling. *International Journal of Plasticity*.

Sun P. L., Cerreta E. K., Gray G. T. III, and Bingert J. F. 2006. The effect of grain size, strain rate, and temperature on the mechanical behaviour of commercial purity aluminum. *Metallurgical and Materials Transactions A* 37A:2983–2994.

Tsou P., Brownlee D. E., Sandford S. A., Hörz F., and Zolensky M. E. 2003. Wild-2 and interstellar sample collection and Earth return. *Journal of Geophysical Research* 108, doi:E10:SRD 3-1.

Tuzzolino A. J., Economou T. E., McKibbon R. B., Simpson J. A., McDonnell J. A. M., Burchell M. J., Vaughan B. A. M., Tsou P., Hanner M. S., Clark B. C., and Brownlee D. E. 2003. Dust flux monitor instrument for the Stardust mission to comet Wild 2. *Journal of Geophysical Research* 108:1–24.

Tuzzolino A. J., Economou T. E., Clark B. C., Tsou P., Brownlee D. E., Green S. F., McDonnell J. A. M., McBride N., and Colwell M. T. S. H. 2004. Dust measurements in the coma of comet 81P/Wild 2 by the dust flux monitor instrument. *Science* 304:1776–1780.

Weissman P. R. and Lowry S. C. 2008. Structure and density of cometary nuclei. *Meteoritics & Planetary Science* 43:1033–1047.

Westphal A. J., Bastien R. K., Borg J., Bridges J., Brownlee D. E., Burchell M. J., Cheng A. F., Clark B. C., Djouadi Z., Floss C., Franchi I., Gainsforth Z., Graham G., Green S. F., Heck P. R., Hor'anyi M., Hoppe P., Hörz F., Joachim Huth J., Kearsley A., Leroux H., Marhas K., Nakamura-Messenger K., Sandford S. A., See T. H., Stadermann F., Tsitrin S., Tsou P., Warren J. L., Wozniakiewicz P. J., and Zolensky M. E. 2008. Discovery of non-random spatial distribution of impacts in the Stardust cometary collector. *Meteoritics & Planetary Science* 43:415–429.

Wozniakiewicz P. J., Kearsley A. T., Burchell M. J., Foster N. J., Cole M. J., Bland P. A., and Russell S. S. 2009. Analyses of residues resulting from laboratory impacts into aluminum 1100 foil: Implications for Stardust crater analyses. *Meteoritics & Planetary Science* 44:1541–1560.

APPENDIX

Protocols for Stardust Small Crater Surveys

The protocols for crater searching on Stardust cometary dust collector foils by SEM were developed and tested by members of the PE foil subteam during the 2 yr prior to sample return, based upon assumed numbers of impacts from DFMI data. It was assumed that optical microscopy of the surface of the whole dust collector would suffice to identify samples for further, more detailed analysis. After the sample return, on the first (optical microscope) examination in the Johnson Space Center, it became apparent that higher magnification and spatial resolution surveys would be necessary, and a second relatively strict protocol was defined to establish the finer particle total fluence. On selected foils, areas of 1 mm^2 were thoroughly examined to locate and measure top-lip diameter for all detectable craters. In practice, it is likely that all craters of >1 μm diameter within the randomly chosen areas were located and measured, but below 1 μm diameter, it is probable that the efficiency of detection varied between investigators, as a function of the instrumentation used.

Collated PE Phase Small Crater Data

Included in the following tables are the collated small crater data from the PE phase of the Stardust mission. There is one table per foil, except for foils for which fewer than four craters were discovered which have been collated together into Table A13.

The given accuracy is that quoted from the various investigators.

Table A1 provides an explanatory key to the various symbols used in the tables. D_p is the inferred projectile diameter as calculated using the calibration described herein. Note, this is not meant to be an inference to the density of the projectile but rather to save the reader time in calculating the diameter based upon this calibration.

Blank cells in Tables A2–A13 indicate that either any residue was below the detection limit of the instrument being used, or no measurement was made.

Figure A1 is a histogram showing the crater diameter data from Tables A2–A13 binned into 0.2 μm bins.

Table A1. Key to symbols used in Tables A2–A13.

Symbol	Meaning
D_c	Crater lip-to-lip diameter
D_p	Inferred projectile diameter using the calibration described herein
# EDX	Number of craters for which a detectable EDX residue was reported
m	Magnesium and iron (mafic) silicate
su	Sulfide (probably iron)
m su	Probably both silicate and sulfide
Ni	Nickel detected in sulfide
Ca	Calcium detected
Na	Sodium detected
Si	Silicon detected (not Mg, etc.), could be inclusion
Fe	Iron detected (not Si, etc.), probably inclusion
C	High carbon noted
Cl	High chlorine noted
K	High potassium noted
S	High sulfur noted
C O	High carbon and oxygen noted
Mg	High magnesium noted
Ca	High calcium noted
Cr	High chromium noted

Table A2. Summary of small crater data from foil C2008N,1 (investigator: Bridges). "EDX" refers to the residue(s) found in the crater by EDX analyses. A key to the symbols can be found in Table A1.

D_c (μm)	D_p (nm)	EDX	D_c (μm)	D_p (nm)	EDX	D_c (μm)	D_p (nm)	EDX
0.12	75		1.1	688		1.6	1000	
0.13	81		1.1	688	su	1.7	1063	
0.13	81		1.1	688	m su	1.7	1063	
0.13	81		1.1	688	su	1.8	1125	m
0.13	81		1.1	688	su Si	1.8	1125	su
0.13	81		1.1	688	Fe Si	1.8	1125	Fe Si
0.15	94		1.2	750		1.8	1125	m su
0.15	94		1.2	750		1.8	1125	Cr su Si
0.15	94		1.2	750		1.8	1125	su
0.15	94		1.2	750	m	1.8	1125	m su
0.15	94		1.2	750	m su	1.9	1188	
0.17	106		1.2	750	Fe Si	1.9	1188	Si
0.18	113		1.2	750	Su Si	1.9	1188	m
0.18	113		1.2	750	Su	1.9	1188	su
0.18	113		1.2	750	M su	2	1250	ni su
0.18	113		1.2	750	m	2	1250	m su
0.19	119		1.3	813		2.1	1313	m
0.2	125		1.3	813		2.1	1313	m su
0.22	138		1.3	813		2.1	1313	m
0.26	163		1.3	813	su Si	2.1	1313	su Ca K S Na Cl
0.28	175		1.3	813	su Si	2.2	1375	
0.28	175		1.3	813	su	2.2	1375	
0.29	181		1.3	813		2.2	1375	m
0.3	188		1.3	813		2.2	1375	m su
0.31	194		1.4	875		2.2	1375	Fe
0.33	206		1.4	875		2.2	1375	su
0.35	219		1.4	875		2.2	1375	Cl K Na S Si Fe F
0.35	219		1.4	875	m	2.3	1438	Fe Si

Table A2. *Continued*. Summary of small crater data from foil C2008N,1 (investigator: Bridges). "EDX" refers to the residue(s) found in the crater by EDX analyses. A key to the symbols can be found in Table A1.

D_c (μm)	D_p (nm)	EDX	D_c (μm)	D_p (nm)	EDX	D_c (μm)	D_p (nm)	EDX
0.36	225		1.4	875	Fe	2.3	1438	m su
0.39	244		1.4	875	su Si	2.3	1438	m
0.42	263		1.4	875	su	2.4	1500	su
0.42	263		1.4	875	su	2.4	1500	m su
0.49	306		1.5	938		2.4	1500	Na Si
0.51	319		1.5	938		2.6	1625	
0.52	325		1.5	938	m	2.6	1625	m su
0.61	381	Fe	1.5	938	su	2.6	1625	
0.68	425	su	1.5	938	su	2.8	1750	m su
0.72	450		1.5	938	m	2.8	1750	su Si
0.73	456	Fe	1.5	938	Ca Fe	2.9	1813	Ca m
0.74	463		1.6	1000		2.9	1813	m su
0.75	469		1.6	1000		3.1	1938	m
0.89	556	Fe	1.6	1000		3.3	2063	m su
0.95	594		1.6	1000		3.5	2188	m su
1	625		1.6	1000	m	3.7	2353	Ca m
1	625		1.6	1000	Si	3.8	2391	K Na m su
1	625		1.6	1000	su	4	2467	Na m su
1	625	m su	1.6	1000	Fe Si	4.1	2505	Ca m
1	625	su	1.6	1000	m	4.4	2615	Ca Fe Si
1	625		1.6	1000	Na Cl	4.7	2722	m
1.1	688		1.6	1000	m su	14.5	5413	C Ca m su

Note: # Craters = 150; # EDX = 80.

Table A3. Summary of small crater data from foil C2020W (investigators: Borg, Leroux). "EDX" refers to the residue(s) found in the crater by EDX analyses. A key to the symbols can be found in Table A1.

D_c (μm)	D_p (nm)	EDX	D_c (μm)	D_p (nm)	EDX	D_c (μm)	D_p (nm)	EDX
0.13	81	su	0.71	419	m	1.17	731	
0.23	144		0.71	444	su	1.23	769	su
0.25	156	Fe	0.75	469		1.69	1056	m su
0.34	213	m su	0.75	469		1.77	1106	
0.36	225		0.77	481		1.82	1138	m su
0.38	238	su	0.78	488		1.82	1138	
0.42	263		0.78	488	m su	1.97	1231	m
0.44	275		0.80	500		2.01	1256	m su
0.47	294		0.81	506	m su	2.02	1263	m su
0.48	300		0.81	506	Fe Si	2.09	1306	m
0.50	313		0.82	513		2.32	1450	
0.55	344	su	0.83		m su	2.34	1463	m su
0.55	344		0.84	525		2.84	1775	m su
0.55	344		0.90	563	Si	2.84	1775	
0.57	356		0.90	563		3.10	1938	
0.59	369		0.91	569	m su	3.23	2019	m su
0.59	369		0.91	569	su	3.23	2019	su
0.61	381		0.91	569	m	3.29	2056	m su
0.61	381		0.98	613	m	3.42	2138	m su
0.63	394		0.99	619	m su	3.73	2331	m su
0.66	413		1.04	650				
0.67	419		1.15	719				

Note: # Craters = 64; # EDX = 30.

Table A4. Summary of small crater data from foil C2037N,1 (investigator: Hoppe). "EDX" refers to the residue(s) found in the crater by EDX analyses. A key to the symbols can be found in Table A1.

D_c (μm)	D_p (nm)	EDX	D_c (μm)	D_p (nm)	EDX	D_c (μm)	D_p (nm)	EDX
0.198	124		0.344	215		0.570	356	m su
0.216	135		0.361	226		0.581	363	
0.217	136		0.377	236		0.587	367	
0.223	139		0.377	236	m	0.591	369	m su
0.251	157		0.387	242		0.611	382	m su
0.255	159		0.400	250		0.627	392	su
0.261	163		0.404	253		0.627	392	m
0.263	164		0.409	256		0.633	396	Ni su
0.265	166		0.409	256		0.691	432	m su
0.271	169		0.432	270	m su	0.712	445	su
0.272	170		0.439	274		0.856	535	m
0.279	174		0.457	286	m	0.915	572	
0.282	176		0.475	297		0.940	588	m
0.286	179	m	0.480	300		1.110	694	
0.287	179		0.487	304	m	1.324	828	m
0.304	190		0.488	305		1.860	1163	
0.316	198		0.519	324		3.810	2395	
0.336	210		0.536	335				
0.336	210	m su	0.556	348	m su			

Note: # Craters = 55; # EDX = 18.

Table A5. Summary of small crater data from foil C2044N,1 (investigator: Stadermann). "EDX" refers to the residue(s) found in the crater by EDX analyses. A key to the symbols can be found in Table A1.

D_c (μm)	D_p (nm)	EDX	D_c (μm)	D_p (nm)	EDX	D_c (μm)	D_p (nm)	EDX
0.22	138		0.32	200	su	0.46	288	m su Ni
0.22	138	m su	0.32	200	su	0.47	294	m su
0.23	144	C O	0.33	206	m	0.48	300	Si
0.23	144	su	0.37	231	m su	0.49	306	m su
0.23	144	m su	0.37	231	su	0.51	319	m su
0.24	150	m su	0.38	238	m su	0.52	325	m su
0.24	150	su	0.40	250	su	0.54	338	m su
0.25	156	m su	0.40	250	m su	0.57	356	m su
0.26	163	m su	0.40	250	m su	0.63	394	m su
0.26	163	su	0.42	263	m su Ca	0.63	394	m su
0.26	163	C O	0.42	263	m su	0.80	500	m su
0.28	175	C O	0.43	269	m su	0.82	513	m su
0.29	181	su	0.43	269	m su Na	1.09	681	m su Ca
0.30	188	m su Ni	0.44	275	su	1.30	813	m su
0.32	200	C O	0.45	281	m su			

Note: # Craters = 44; # EDX = 43.

Table A6. Summary of small crater data from foil C2044W,1 (investigator: Hoppe). "EDX" refers to the residue(s) found in the crater by EDX analyses. A key to the symbols can be found in Table A1.

D_c (μm)	D_p (nm)	EDX	D_c (μm)	D_p (nm)	EDX	D_c (μm)	D_p (nm)	EDX
0.16	100	m	0.32	200		0.51	319	
0.18	113	m su	0.34	213		0.63	394	m su
0.22	138	su	0.35	219		0.69	431	
0.23	144	su	0.37	231	m su	0.71	444	m su
0.29	181	m	0.41	256		0.71	444	m su
0.32	200	m su	0.45	281	m su	0.99	619	m

Note: # Craters = 18; # EDX = 12.

Table A7. Summary of small crater data from foil C2052N,1 (investigator: Hoppe). "EDX" refers to the residue(s) found in the crater by EDX analyses. A key to the symbols can be found in Table A1.

D_c (μm)	D_p (nm)	EDX	D_c (μm)	D_p (nm)	EDX	D_c (μm)	D_p (nm)	EDX	D_c (μm)	D_p (nm)	EDX
0.114	71		0.305	191		0.385	241		0.490	306	
0.129	81		0.306	191		0.386	241		0.491	307	
0.131	82		0.307	192		0.388	243		0.505	316	
0.138	86		0.308	193		0.388	243		0.508	318	
0.177	111		0.309	193		0.389	243		0.510	319	
0.182	114		0.312	195		0.389	243		0.521	326	
0.193	121		0.320	200		0.389	243		0.528	330	
0.208	130		0.321	201		0.398	249		0.541	338	
0.213	133		0.322	201		0.399	249		0.551	344	
0.216	135		0.322	201		0.399	249		0.553	346	
0.219	137		0.324	203		0.400	250		0.560	350	m su
0.219	137		0.325	203		0.400	250		0.572	358	
0.230	144		0.329	206		0.404	253		0.586	366	
0.236	148		0.334	209		0.409	256		0.586	366	m su
0.238	149		0.335	209		0.416	260		0.589	368	
0.240	150		0.341	213		0.419	262		0.589	368	
0.242	151		0.345	216		0.421	263		0.606	379	su Si
0.245	153		0.346	216		0.425	266		0.656	410	
0.258	161		0.346	216		0.427	267		0.657	411	
0.260	163		0.349	218		0.428	268		0.705	441	
0.260	163		0.349	218		0.430	269		0.709	443	
0.260	163		0.349	218		0.436	273		0.725	453	m su
0.262	164		0.350	219		0.442	276		0.733	458	
0.264	165		0.352	220		0.446	279		0.737	461	
0.267	167		0.352	220		0.447	279		0.752	470	
0.268	168		0.356	223		0.449	281		0.769	481	m
0.271	169		0.357	223		0.450	281		0.793	496	
0.272	170		0.357	223		0.452	283		0.931	582	
0.276	173		0.362	226		0.454	284		0.940	588	su
0.276	173		0.363	227		0.455	284		0.953	596	
0.278	174		0.363	227		0.456	285		1.001	626	
0.281	176		0.365	228		0.457	286		1.092	683	m su
0.282	176		0.365	228		0.459	287		1.105	691	
0.286	179		0.366	229		0.459	287		1.187	742	m
0.287	179		0.367	229		0.464	290		1.236	773	m su
0.289	181		0.369	231		0.471	294		1.266	791	
0.290	181		0.373	233		0.474	296		1.348	843	
0.292	183		0.373	233		0.474	296		1.517	948	m
0.294	184		0.374	234		0.477	298				
0.301	188		0.377	236		0.483	302				
0.301	188		0.378	236		0.484	303				
0.301	188		0.380	238		0.485	303				

Note: # Craters = 164; # EDX = 10.

Table A8. Summary of small crater data from foil C2054N,1 (investigator: Green). "EDX" refers to the residue(s) found in the crater by EDX analyses. A key to the symbols can be found in Table A1.

D_c (μm)	D_p (nm)	EDX	D_c (μm)	D_p (nm)	EDX	D_c (μm)	D_p (nm)	EDX
0.5	313		0.7	438		1.0	625	
0.5	313		0.7	438		1.1	688	
0.5	313		0.7	438		1.2	750	
0.6	375		0.7	438		1.3	813	Si
0.6	375		0.7	438		1.4	875	Fe Si
0.6	375		0.7	438		1.6	1000	m
0.6	375		0.7	438		1.7	1063	m
0.6	375		0.7	438		1.7	1063	m
0.6	375		0.7	438		2.0	1250	m
0.6	375		0.8	500		2.0	1250	

Table A8. *Continued*. Summary of small crater data from foil C2054N,1 (investigator: Green). "EDX" refers to the residue(s) found in the crater by EDX analyses. A key to the symbols can be found in Table A1.

D_c (μm)	D_p (nm)	EDX	D_c (μm)	D_p (nm)	EDX	D_c (μm)	D_p (nm)	EDX
0.6	375		0.8	500		2.6	1625	m
0.6	375		0.8	500		2.7	1688	
0.7	438		0.8	500		2.8	1750	
0.7	438		0.9	563		12.0	4823	

Note: # Craters = 42; # EDX = 7.

Table A9. Summary of small crater data from foil C2054W,1 (investigator: Graham). "EDX" refers to the residue(s) found in the crater by EDX analyses. A key to the symbols can be found in Table A1.

D_c (μm)	D_p (nm)	EDX	D_c (μm)	D_p (nm)	EDX	D_c (μm)	D_p (nm)	EDX
0.104	65		0.412	258		0.839	524	
0.181	113		0.422	264		0.965	603	Ni su
0.222	139		0.430	269		1.050	656	m su
0.303	189		0.487	304		1.170	731	m su
0.311	194		0.519	324		1.240	775	m su
0.328	205		0.536	335		1.740	1088	m su
0.331	207		0.550	344		1.800	1125	m su
0.350	219		0.607	379		2.950	1844	m su
0.396	248		0.616	385		7.950	3752	m su
0.404	253		0.684	428	m su			

Note: # Craters = 29; # EDX = 9.

Table A10. Summary of small crater data from foil C2060W,1 (investigator: Green). "EDX" refers to the residue(s) found in the crater by EDX analyses. A key to the symbols can be found in Table A1.

D_c (μm)	D_p (nm)	EDX	D_c (μm)	D_p (nm)	EDX	D_c (μm)	D_p (nm)	EDX
0.5	313		0.6	375		0.9	563	
0.6	375		0.7	438		1.0	625	
0.6	375		0.8	500		9.0	4046	m su

Note: # Craters = 9; # EDX = 1.

Table A11. Summary of small crater data from foil C2068W,1 (investigators: Borg, Leroux). "EDX" refers to the residue(s) found in the crater by EDX analyses. A key to the symbols can be found in Table A1.

D_c (μm)	D_p (nm)	EDX	D_c (μm)	D_p (nm)	EDX	D_c (μm)	D_p (nm)	EDX
0.44	275	su	0.82	513		1.32	825	su
0.57	356		0.95	594		1.54	963	m
0.75	469	m	0.98	613		1.57	981	m
0.77	481		1.08	675		1.74	1088	m
0.82	513	m						

Note: # Craters = 13; # EDX = 7.

Table A12. Summary of small crater data from foil C2100N,1 (investigator: Graham). "EDX" refers to the residue(s) found in the crater by EDX analyses. A key to the symbols can be found in Table A1.

D_c (μm)	D_p (nm)	EDX	D_c (μm)	D_p (nm)	EDX	D_c (μm)	D_p (nm)	EDX
0.145	91		0.258	161		0.339	212	
0.152	95		0.264	165		0.341	213	
0.172	108		0.281	176		0.354	221	
0.181	113		0.284	178		0.357	223	
0.183	114		0.288	180		0.428	268	
0.184	115		0.294	184		0.438	274	
0.199	124		0.301	188		0.448	280	
0.212	133		0.303	189		0.475	297	m su
0.250	156		0.308	193		0.486	304	
0.254	159		0.309	193		0.595	372	
0.257	161		0.319	199		0.910	569	m su
0.258	161		0.321	201				

Note: # Craters = 35; # EDX = 2.

Table A13. Summary of small crater data from foils C2043N,1 (investigators: Borg, Stroud [FIB]); C2125N,1 (investigators: Green, Kearsley); C2051N,1 (investigator: Green); C2126W,1 (investigator: Hoppe); and C2114N,1 (investigators: Borg, Leroux). "EDX" refers to the residue(s) found in the crater by EDX analyses. A key to the symbols can be found in Table A1.

D_c (μm)	D_p (nm)	EDX
C2043N,1[a]		
0.275	172	
1.47	919	m su
1.76	1100	m su
C2125N,1[b]		
2.4	1500	m su Ca
4.6	2687	m su C
9.1	4074	m su Si C
C2051N,1[c]		
0.9	563	
6.7	3380	Mg Fe Si Ca Ti Cl
C2126W,1[d]		
0.27	169	
0.37	231	
C2114N,1[e]		
1.12	700	
1.29	806	
1.64	1025	

[a]# Craters = 3, # EDX = 2.
[b]# Craters = 3, # EDX = 3.
[c]# Craters = 2, # EDX = 1.
[d]# Craters = 2, # EDX = 0.
[e]# Craters = 3, # EDX = 0.

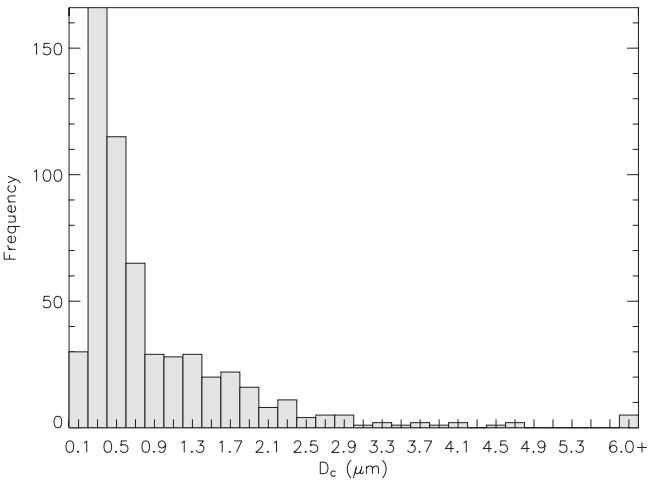

Fig. A1. Crater size distribution for all crater data in Tables A2–A13. Bars are 0.2 μm in width. The last bar (labeled "6.0+") is the sum of craters with a diameter ≥6.0 μm.